An Investigation of the Effects of Ductile-Layer Thickness on the Fracture Behavior of Nickel Aluminide Microlaminates

M. LI and W.O. SOBOYEJO

This article presents the results of a combined experimental and analytical study of the effects of ductile-layer thickness on the initiation toughness and resistance-curve behavior of nickel aluminide composites that are reinforced with ductile V and Nb-15Al-40Ti layers. The initiation toughness and specimen-independent steady-state toughness values are shown to increase with increasing layer thickness. Stable crack growth and toughening in the crack-arrestor orientation are also attributed to crack bridging and the interactions of crack tips with the ductile layers. The overall toughening in the microlaminates is modeled by superposing the shielding contributions due to crack bridging on the stress-intensity factor required to promote renucleation ahead of the first ductile layer ahead of the precrack. The implications of the results are also discussed for the design of ductile phase–toughened microlaminates.

I. INTRODUCTION

SINCE the pioneering work of Krstic *et al.*,[1,2] considerable effort has been made to utilize the concept of ductile-phase toughening in the design of toughened composite systems.[3–22] Much of the early work was performed on composites reinforced with ductile particles[3–6] or fibers[4,6–11] which were chosen to promote toughening, largely by crack bridging.[3–11] The early studies showed that fiber-reinforced composites generally promote greater levels of toughening than particulate-reinforced composites. However, subsequent work on ductile layer–reinforced composites[4,12–22] soon revealed that such composite architectures result in even greater levels of toughening than ductile fiber–reinforced brittle matrix composites.[4,6–11] The interest, in recent years, has, therefore, shifted toward an understanding of the effects of ductile-layer thickness on the fracture toughness of brittle matrix composites.[12–22]

This article presents the results of fundamental studies of the effects of ductile-layer thickness on the fracture-initiation toughness and resistance-curve behavior of nickel aluminide microlaminates. Model composites reinforced with 20 vol pct of ductile vanadium layers (100, 200, and 400 μm thicknesses) or ductile Nb-15Al-40Ti layers (100, 500, and 1000 μm thicknesses) were used in this study. The ductile-phase reinforcements were selected due to their compatibility with NiAl, which was demonstrated in unpublished diffusion-couple studies by the authors in the same processing temperature regime (~1100 °C). The vanadium and Nb-15Al-40Ti were also investigated, since they exhibit essentially elastic–perfectly plastic behavior. Furthermore, the partially ordered B2 Nb-15Al-40Ti intermetallic[23] (all compositions quoted in atomic percent unless stated otherwise) layers exhibit attractive combinations of damage tolerance and oxidation resistance in the intermediate-temperature regime (650 °C to 850 °C).[23,24]

As in recent studies by Bloyer *et al.*[12,13] on similar layered composites, fracture-initiation toughness and resistance-curve behavior in the model composite systems are shown to improve with increasing layer thickness in the crack-arrestor orientation. The intrinsic steady-state toughness values were also shown to increase with increasing ductile-layer thickness. However, the results indicate that fracture instability is more likely to occur at smaller crack extensions, as the ductile-layer thickness is increased. The initiation toughness, resistance-curve behavior, and steady-state toughness levels are predicted with micromechanics models. The implications of the results are then discussed for the design and potential applications of brittle matrix composites reinforced with ductile layers.

II. MICROMECHANICAL MODELING

Following the example of Budiansky *et al.*[25] and Rose,[26] the individual ductile layers within a bridged crack may be modeled as springs (Figure 1), with effective spring stresses that are given by

$$\sigma = \frac{kE\nu}{1 - v^2} \qquad [1]$$

where ν is the crack-face displacement, E is the Young's modulus, v is the Poisson's ratio, and k is a dimensionless spring-stiffness coefficient. The effective spring constant for the bridged-layer configurations may be estimated by considering the pinning of the crack by a single isolated layer in a dilute composite with a relatively low volume fraction (c) of layers, in which interactions between individual layers can be neglected (Figures 2(a) and (b)). The remote displacement of the crack in Figure 2(a) may be estimated by invoking the analogy between the crack-opening profile and the displacement profile due to a smooth punch. This is given by Johnson[27] to be

$$\nu = \frac{\alpha\sigma_p(1 - v_m^2)}{E_m} \qquad [2]$$

M. LI, formerly Graduate Research Associate, Department of Materials Science and Engineering, The Ohio State University, is Process Engineer, Huffman Corporation, Lake Wylie, SC 29710. W.O. SOBOYEJO, formerly Associate Professor, Department of Materials Science and Engineering, The Ohio State University, Columbus, OH, is Professor, Princeton Materials Institute and the Department of Mechanical and Aerospace Engineering, Princeton University, Princeton, NJ 08544.

Manuscript submitted June 15, 1999.

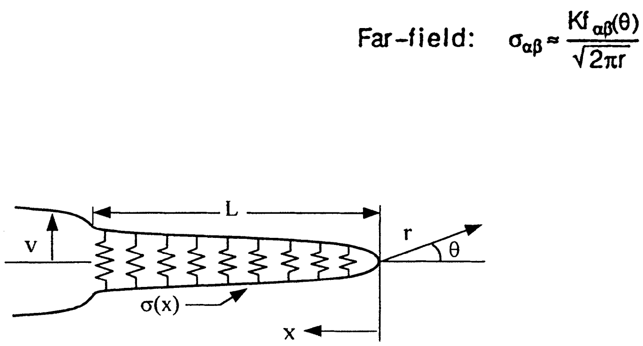

Fig. 1—Schematic illustration of bridging-spring model.[25]

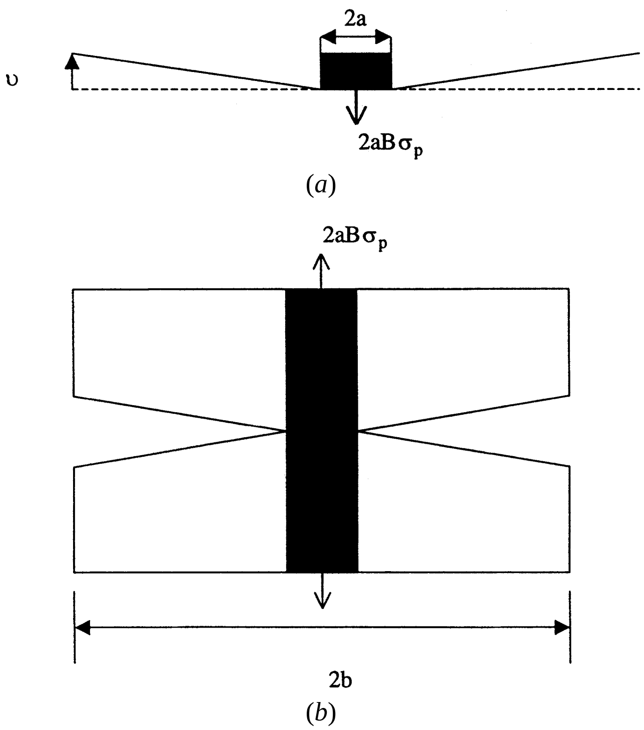

Fig. 2—Idealization of crack-opening profile due to ductile layer bridging: (*a*) $c \rightarrow 0$ and (*b*) $c = a/b$.

where

$$\alpha = \frac{(a+b)\ln\left(1+\frac{b}{a}\right)^2 + (a-b)\ln\left(1-\frac{b}{a}\right)^2}{\pi} \qquad [3]$$

where a is the half-thickness of the ductile layer and b is chosen to satisfy $a/b = c$; E_m and v_m are the Young's modulus and Poisson's ratio of the matrix, respectively; and σ_p is the average layer stress. Equation [2] corresponds essentially to the layer/crack configuration in a half-space for which $c \rightarrow 0$ (Figures 2(a) and (b)). Note that c also corresponds to the layer volume fraction for the unit cell shown in Figure 2(b). Also, the positive x direction in Figure 2(b) may be considered to be from either end of the unit cell (right or left) toward the central layer.

Following the methods of Budiansky *et al.*,[25] the average crack-opening displacement (ν_{ave}) may also be estimated for arbitrary values of c to be

$$\nu_{\text{ave}} = \beta(c)\,\frac{\alpha\sigma_p\,(1-v_m^2)}{E_m} \qquad [4]$$

where α, $\beta(c)$ is a correction factor for the solution of a crack in a half-space (Figure 2(a)), presented in Eq. [2]. The variations of $\beta(c)$ with ductile-layer volume fraction may be estimated using the stress-intensity-factor solutions for a double-edged crack solid provided by Tada *et al.*[28] This gives

$$K_I = \sigma\sqrt{\pi(b-a)}\,F\left(1-\frac{a}{b}\right) \qquad [5]$$

where

$$F\left(1-\frac{a}{b}\right) = \frac{1.122 - 0.561\left(1-\frac{a}{b}\right) - 0.205\left(1-\frac{a}{b}\right)^2 + 0.471\left(1-\frac{a}{b}\right)^3 - 0.190\left(1-\frac{a}{b}\right)^4}{\sqrt{\frac{a}{b}}} \qquad [6]$$

where $\sigma = c\sigma_p$ is the applied stress. The elastic strain energy released (R) by cutting the crack into the block (Figure 2(b)) in the presence of constant σ is given by

$$R = \int_a^b \frac{K_I^2\,(1-\nu_m^2)}{E_m}\,B\,dx \qquad [7]$$

where B is the thickness of the block. The term R may also be equated to $2Bb\sigma\nu_{\text{ave}}$. Hence, ν_{ave} may be found by equating the previous expression to Eq. [7]:

$$\nu_{\text{ave}} = \frac{\int_a^b \frac{K_I^2\,(1-v_m^2)}{E_m}\,dx}{2b\sigma} \qquad [8]$$

By equating ν_{ave} from Eq. [8] to Eq. [4], $\beta(c)$ is found to be

$$\beta(c) = \frac{\pi^2\int_c^1 (1-\rho)\,(F\,(1-\rho))^2\,d\rho}{2\left(\left(1+\frac{1}{c}\right)\ln\left(1+\frac{1}{c}\right)^2 + \left(1-\frac{1}{c}\right)\ln\left(1-\frac{1}{c}\right)^2\right)} \qquad [9]$$

We may now estimate ν_{ave} by substituting the result for $\beta(c)$ (from Eq. [9]) into Eq. [4]. Following this, substituting $\nu = \nu_{\text{ave}}$ into Eq. [1] gives the following relationship for the dimensionless spring-stiffness coefficient:

$$k = \frac{c}{\beta\alpha}\,\frac{E_m}{1-v_m^2}\,\frac{1-v^2}{E} \qquad [10]$$

where E and v are the effective Young's modulus and Poisson's ratio of the composite materials, respectively.

The previous derivation for elastic springs may be extended to the case of elastic-plastic springs by assuming an elastic–perfectly plastic behavior of the ductile layer, for which (Figure 3)

$$\sigma = \frac{kE\nu}{1 - \nu^2} \text{ for } \nu \leq \nu_y = \frac{\sigma_y(1 - \nu^2)}{kE}$$
$$= \sigma_y \text{ for } \nu \geq \nu_y \quad [11]$$

Hence, if $\nu(L)$ at the end of the bridged zone exceeds ν_y, the J-integral result for the toughening due to crack bridging generalizes to[25]

$$\frac{(1 - \nu^2)K^2}{E_c} = \frac{(1 - \nu_m^2)\,K_m^2}{E_m} + \frac{(1 - \nu^2)\sigma_y^2}{kE} + 2\sigma_y\,(\nu(L) - \nu_y) \quad [12]$$

where the subscript m corresponds to the matrix. If failure of the last spring is assumed to occur when $\nu(L)$-ν_y reaches a critical plastic value (ν_p), the toughening ratio (λ) becomes[25]

$$\lambda = \frac{K}{K_m} = \left(1 + \frac{\sigma_y^2}{kK_m^2}\left(1 + \frac{2\nu_p}{\nu_y}\right)\right)^{1/2} \quad [13]$$

where K_m is the matrix toughness. The result can be rearranged to give the estimation of toughening (ΔK_b) due to ductile layer bridging:

$$\Delta K_b = (\lambda - 1)K_m \quad [14]$$

Equations [13] and [14] can be used to estimate the steady-state fracture toughness of a brittle matrix reinforced with ductile layers. However, the aforementioned modeling framework cannot readily be used to predict the resistance-curve behavior due to crack bridging, since it does not include a bridging-length scale. This can be accomplished by considering the increase in the stress-intensity factor due to large-scale bridging (LSB) conditions.

Under such conditions, the lengths of bridging zones are generally observed to be comparable to the overall crack dimensions.[12–14,22] Large scale bridging models[12–14,18,26–28] are also needed to estimate the shielding contributions from crack bridging. The early LSB models were first formulated by Odette *et al.*[18] and Zok and Hom.[29] Subsequent work by Cox and co-workers[30,31] also established self-consistent methods for the analysis of large-scale crack bridging. However, these LSB models often require iterative methods/algorithms that may sometimes have convergence problems associated with them.

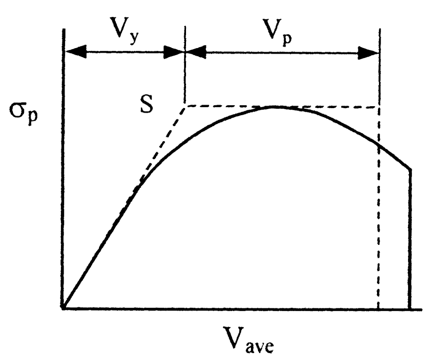

Fig. 3—Stress *vs* average displacement showing elastic–perfectly plastic behavior of ductile layer.[25]

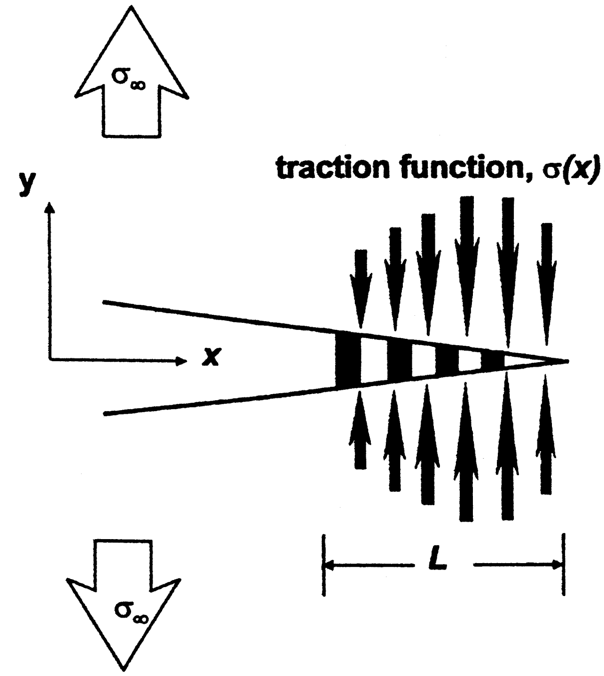

Fig. 4—Schematic representation of a large-scale bridging model.[13]

A simpler LSB model was, therefore, employed in the current study. This model, which was first proposed by Bloyer *et al.*[13,14] utilizes weight functions by Fett and Munz[32] in the estimation of the weighted distributions of bridging traction across the individual reinforcements (Figure 4). The shielding due to LSB (ΔK_{lsb}) may, thus, be expressed as

$$\Delta K_{\text{lsb}} = \int_L \gamma\sigma(x)h\,(a, x)\,dx \quad [15]$$

where L is the length of the bridge zone, γ is a constraint/triaxiality factor, $\sigma(x)$ is a traction function along the bridge zone, and $h\,(a, x)$ is a weight function given by Fett and Munz:[32]

$$h(a, x) = \sqrt{\frac{2}{\pi a}}\frac{1}{\sqrt{1 - \frac{x}{a}}}\left(1 + \sum_{(\nu,\mu)} \frac{A_{\nu\mu}\left(\frac{a}{W}\right)}{\left(1 - \frac{a}{W}\right)}\left(1 - \frac{x}{a}\right)^{\nu+1}\right) \quad [16]$$

where a is the crack length and W is the specimen width. The coefficients ($A_{\nu\mu}$) are given in Table I for a single

Table I. Coefficients of Fit Polynomial for SENB Specimen

	μ				
ν	0	1	2	3	4
0	0.4980	2.4463	0.0700	1.3187	−3.067
1	0.5416	−5.0806	24.3447	−32.7208	18.1214
2	−0.19277	2.55863	−12.6415	19.7630	−10.986

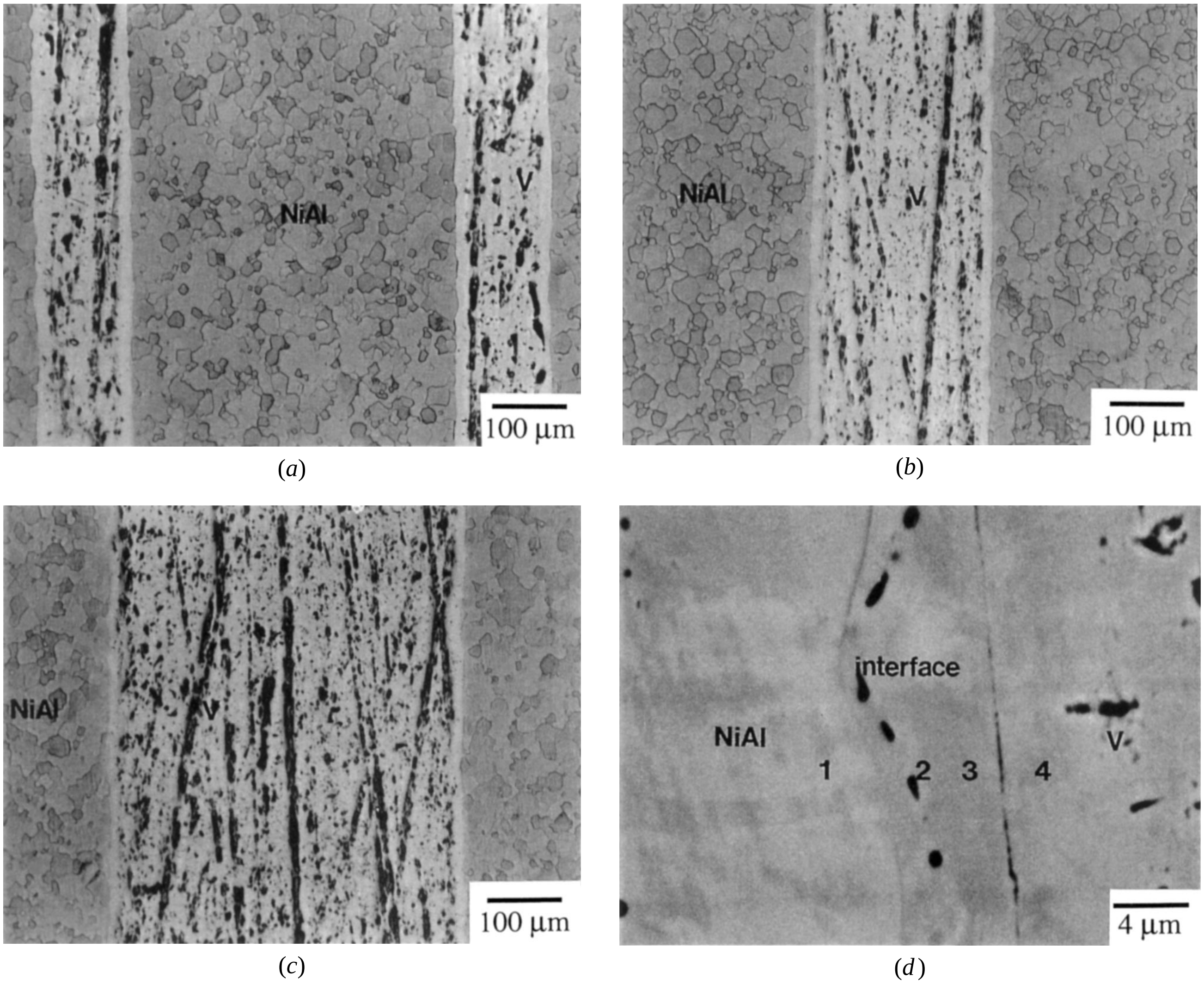

Element	Composition (mole %)			
	1	2	3	4
Ni	51.3	10.5	13.0	0.8
Al	48.7	10.7	12.5	0
V	0	78.8	74.5	99.2

Fig. 5—Typical microstructure of NiAl/V composites: optical micrograph of NiAl composites reinforced with (*a*) 100-μm-thick V layer, (*b*) 200-μm-thick V layer, and (*c*) 400-μm-thick V layer. (*d*) SEM micrograph of the interface between NiAl and V layers.

edge notched bend (SENB) specimen. The resistance-curve behavior may now be estimated by a simple application of the principle of linear superposition. This gives the following expression for the estimation of the stress-intensity factors along the resistance curve:

$$K_{\text{lsb}} = K_i + \Delta K_{\text{lsb}} \qquad [17]$$

where K_i is the initiation toughness required for renucleation ahead of the first ductile layer encountered by the propagating crack, and ΔK_{lsb} is given by Eq. [17] for LSB.

III. MATERIAL

The −325 mesh (25 to 30 μm average size) NiAl powders that were used in this study were procured from Homogeneous Metals, Inc. (Clayville, NY). The vanadium strips, with thicknesses of 100, 200, and 400 μm, were supplied by Fine Metals Corp. (Ashland, VA), while the Nb-15A1-40Ti strips, with thicknesses of 100, 500, and 1000 μm, were produced by Teledyne Wah Change (Albany, OR). Model NiAl composites reinforced with 20 vol pct of V or Nb-15Al-40Ti layers were produced by manual lay-up of NiAl powders on the layered reinforcements inside stainless steel cans. After manual lay-up, the cans were evacuated and sealed by electron-beam welding. The evacuated cans were then hot isostatically pressed under 207 MPa pressure at 1100 °C for 4 hours.

Typical microstructures of the NiAl/V microlaminates are presented in Figures 5(a) through (d). These show distributions of vanadium layers in a matrix of NiAl. The dark spots on the micrographs are polishing artifacts. The average size of NiAl grains measured by image analysis was about 25 μm. A small 5- to 10-μm-thick interfacial layer was also observed to form between the NiAl and vanadium layers

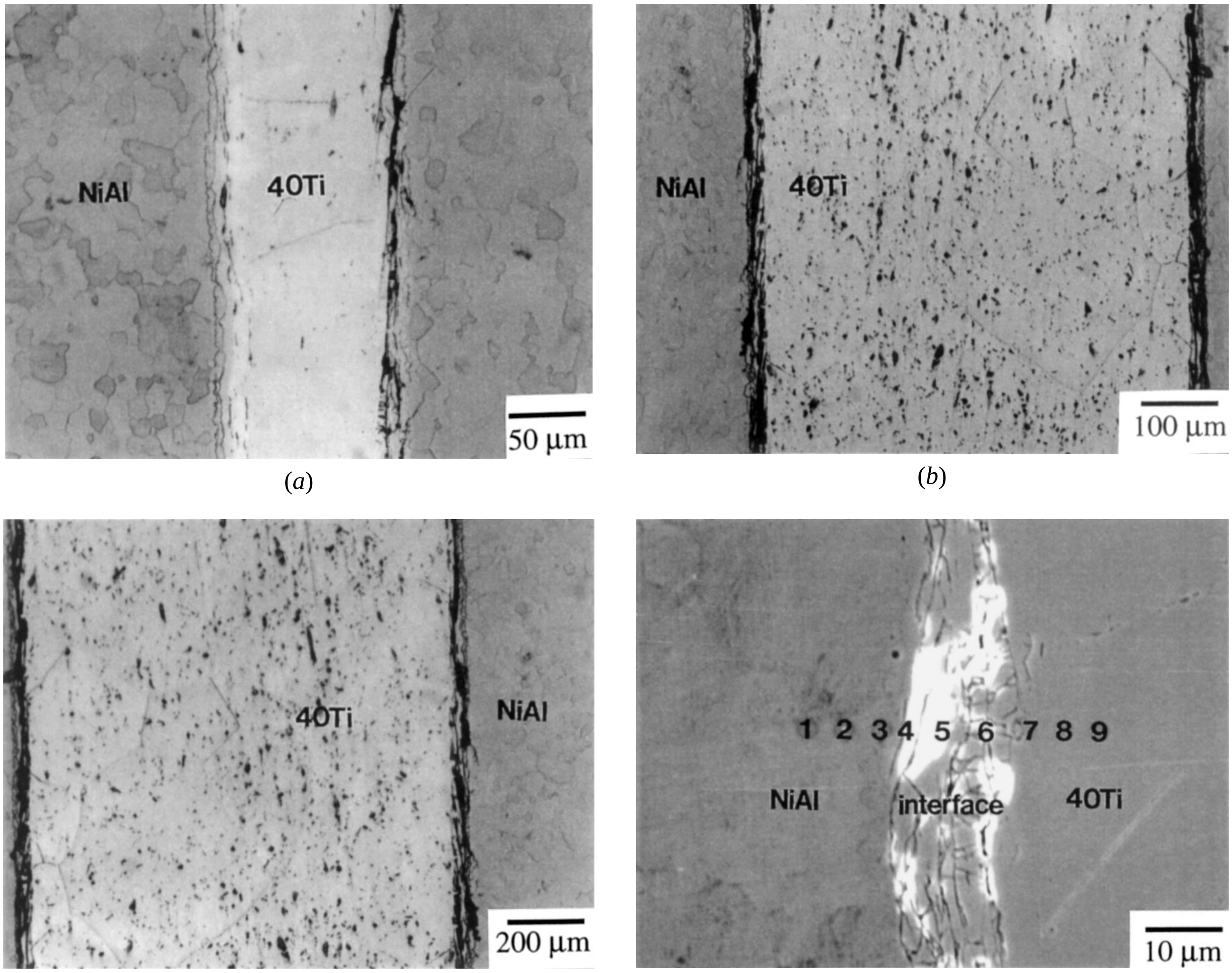

(*a*) (*b*) (*c*) (*d*)

Element	Composition (mole %)								
	1	2	3	4	5	6	7	8	9
Ni	50.1	50.6	49.4	59.5	5.7	6.1	2.7	1.8	1.9
Al	48.7	45.6	24.9	9.4	25.6	21.9	14.1	14.7	14.7
Nb	0.1	0.1	1.8	11.9	45.8	45.8	46.9	47.1	47.1
Ti	1.1	3.7	23.9	19.2	22.9	26.2	36.3	36.4	36.3

Fig. 6—Typical microstructure of NiAl/Nb-15Al-40Ti (40Ti) composites: optical micrograph of NiAl composites reinforced with (*a*) 100-μm-thick Nb-15Al-40Ti layer, (*b*) 500-μm-thick Nb-15Al-40Ti layer, and (*c*) 1000-μm-thick Nb-15Al-40Ti layer. (*d*) SEM micrograph of the interface between NiAl and Nb-15Al-40Ti layers.

(Figure 5(d)). Semiquantitative energy-dispersive X-ray (EDX) spectroscopy revealed that this layer consisted of ~11.8 at. pct Ni, ~11.6 at. pct Al, and ~76.6 at. pct V. Some roughening was also observed at the interfaces between the interfacial layers and the NiAl or 40Ti layers.

Typical microstructures of the NiAl/Nb-15Al-40Ti composites are presented in Figures 6(a) through (d). As in the NiAl/V composites (Figures 5(a) through (d)), some roughening was observed at the interfaces between the different layers. Also, a more-complex reaction zone of approximately 15 to 20 μm in thickness was observed to form between the NiAl and the Nb-15Al-40Ti layers (Figure 6(d)). The EDX analyses showed that the average composition of the reaction interface is ~5.9 at. pct Ni, ~23.8 at. pct Al, ~45.8 at. pct Nb, and 24.5 at. pct Ti. It is important to note here that the compositions obtained *via* EDX are semiquantitative in nature. Nevertheless, they do provide a clear indication of the significant differences between the layer compositions (Figures 5 and 6).

The measured constituent mechanical properties[22,23] (which were assumed to be isotropic) used in the shielding estimations are summarized in Table II. However, it is also important to note here that the constituent mechanical properties may also be affected by the interdiffusion of interstitial oxygen which occurs during processing in stainless steel cans that were evacuated only to pressures of 10^{-4} Pa. These

Table II. Material Properties of NiAl, V, and Nb-15Al-40Ti

MaterialProperty	NiAl[22]	V[22]	Nb-15Al-40Ti[23]
Young's modulus E (GPa)	188	103	101
Possion's ratio ν	0.31	0.36	0.30
Yield stress σ_y (MPa)	—	447	568
Constrained plastic strain/elastic strain (ν_p/ν_y)	—	3	1

may reduce the ductilities of the vanadium layers and, in some cases, result in cleavage-fracture components within the latter. The constituent properties listed in Table II are, therefore, acknowledged to be estimates of the actual layer properties.

IV. EXPERIMENTAL

The initiation fracture toughness and the resistance-curve behavior of the NiAl/V and NiAl/Nb-15Al-40Ti microlaminates were studied using 38.1-mm-long SENB specimens with rectangular cross sections (with a width of 15.24 mm and a thickness of 6.35 mm). The specimens were fabricated *via* electrodischarge machining. The sides of the specimens were diamond polished prior to precracking under cyclic compression. After precracking, the SENB specimens were loaded in incremental stages under three-point bending until crack initiation was observed from the precracks. The loads were then increased in 2 to 5 pct increments to promote stable crack growth until specimen fracture occurred.

The crack/microstructure interactions associated with stable crack growth were monitored with an optical microscope before each load increment. This was continued until unstable crack growth/fracture occurred during incremental loading. As a control, the fracture toughness of monolithic NiAl was also measured using SENB specimens of the same dimensions. Fracture modes in the failed specimen were also investigated using scanning electron microscopy.

V. RESULTS

A. *NiAl/V Composites*

In all NiAl/V composites, matrix crack initiation occurred in the NiAl at the matrix toughness level of ~6.6 MPa$\sqrt{\text{m}}$. However, the propagating cracks in the NiAl layers were retarded by the ductile vanadium layers (Figures 7(a) and (b)). Subsequent crack growth, therefore, involved the reinitiation of cracks in the adjacent interfacial layers, as shown in Figure 7(b). Note that the cracks were bridged by the vanadium layers, as they propagated through the NiAl/V composites. Also, although the vanadium layers were deformed plastically, none of them were observed to fracture during the development of LSB zones. Furthermore, fracture of the vanadium layers was only observed to occur at the onset of catastrophic failure.

A similar sequence of events was observed in all the composites (100-, 200-, and 400-μm-thick layers) that were examined (Figures 8(a) through (c)). The crack/microstructure interactions illustrated in Figures 7(a) and (b) are, therefore, comparable to those of all the other composites. It is also important to note here that the propagating cracks stopped when they reached the vanadium layers (Figure

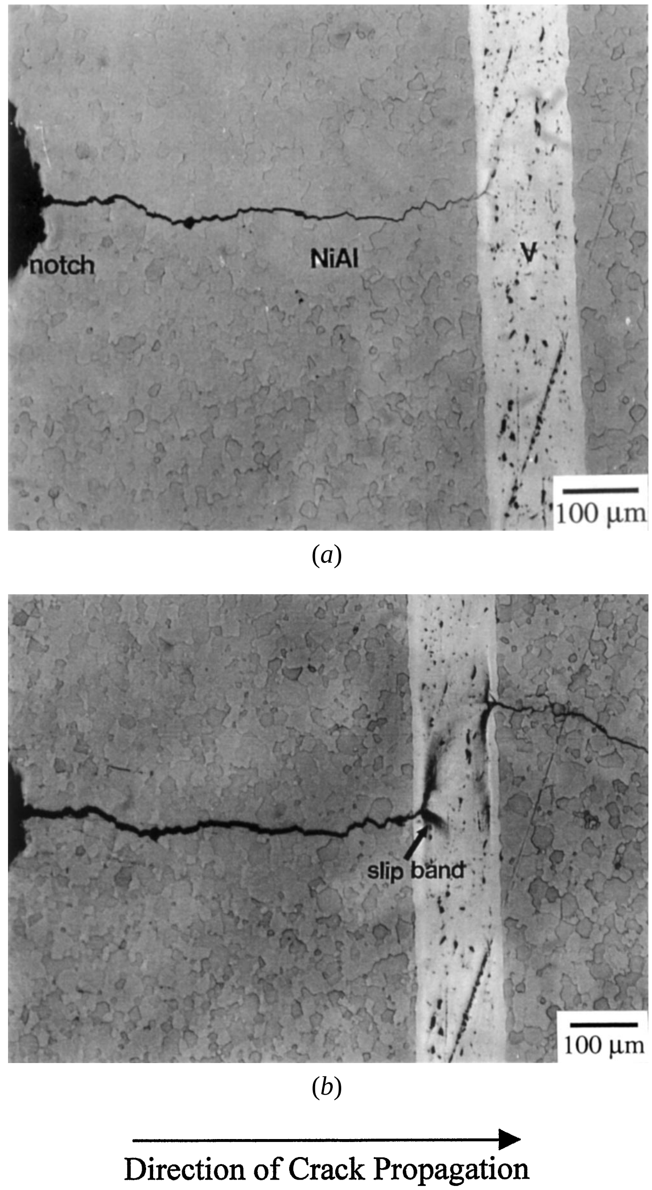

(*a*) (*b*)

Fig. 7—Crack propagation in NbAl/V composites: (*a*) retardation of the crack and formation of the slip band and (*b*) reinitiation of the propagating crack.

7(a)). The measured resistance curves, therefore, correspond to the interceptions of the propagating cracks with the ductile vanadium layers. Furthermore, a small plastic zone and some debonding were then observed in the vanadium, as the load was increased in an effort to reinitiate crack growth in the composites (Figure 7(a)). Slip bands were observed to form along the ~45 deg orientation on both sides of the vanadium

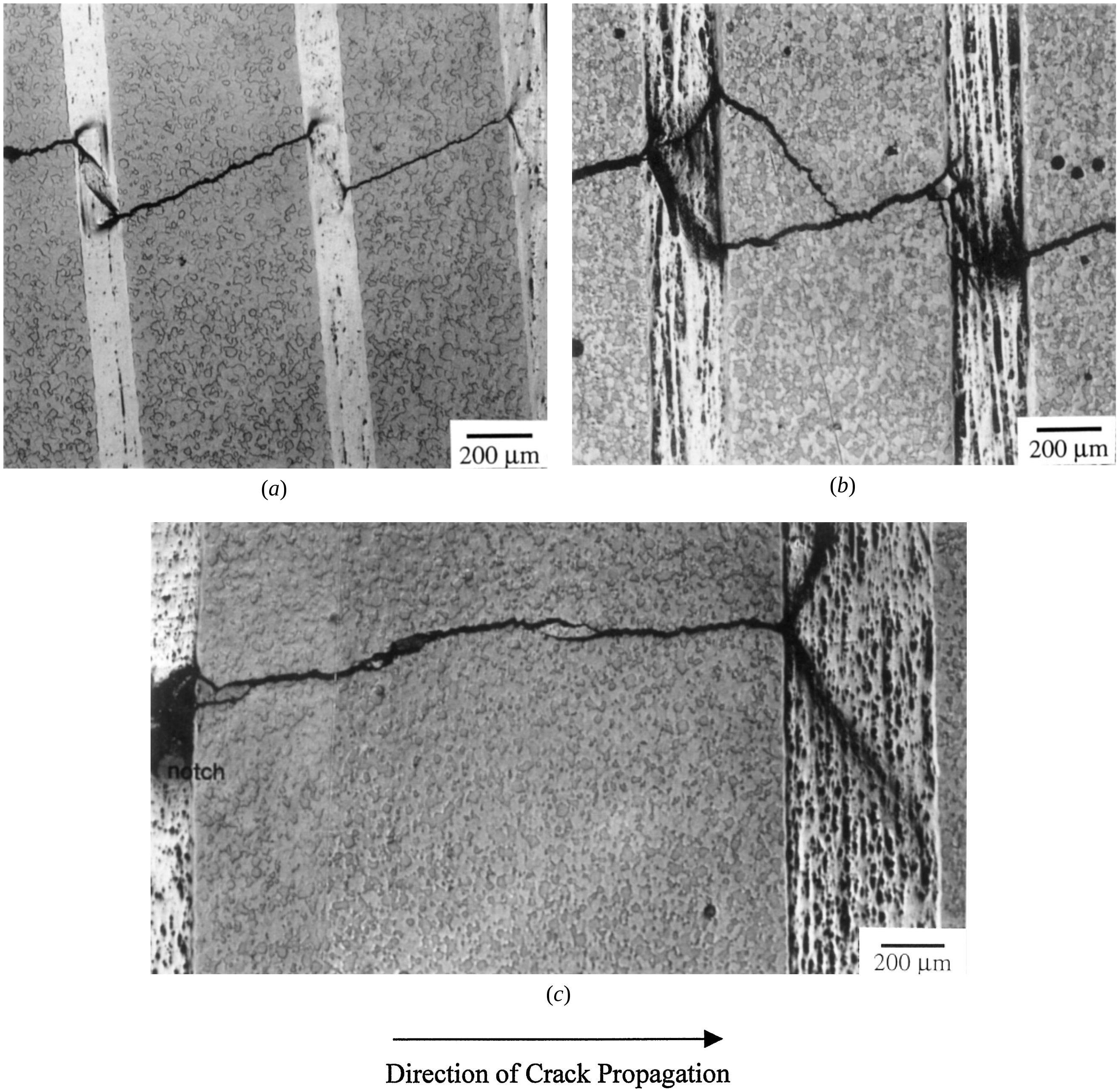

Fig. 8—Crack/microstructure interactions in NiAl/V composites reinforced with (*a*) 100-μm-thick vanadium layer, (*b*) 200-μm-thick vanadium layer, and (*c*) 400-μm-thick vanadium layer.

layers, as the load was increased further (Figure 7(b)). Finally, stable crack growth was observed to renucleate from the slip bands into the adjacent interfacial layers, as shown in Figures 7 and 8. In all cases, reinitiation occurred at a point that was offset somewhat from the initial mode I direction (Figure 7(b)). This offset position, corresponding to an angle of ~45 deg to the initial mode I direction, is consistent with the positions of peak maximum shear strain that were computed in the detailed finite-element simulation of the same NiAl/V composite systems.[22]

Subsequent crack growth occurred along the deflected direction (~30 deg from the pure mode I direction), as shown in Figures 8(a) and (b), for composites reinforced with 100- and 200-μm-thick vanadium layers. Unfortunately, however, renucleation in the case of the composites containing 400-μm-thick layers (Figure 5(c)) resulted in unstable crack growth and catastrophic failure. Also, the onset of unstable crack growth and catastrophic failure in the composites reinforced with 400-μm-thick vanadium layers was associated with relatively high load increments (compared to those in the composites reinforced with 100- and 200-μm-thick vanadium layers, where renucleation of stable crack growth occurred in NiAl layers adjacent to the vanadium layers). The rates of change of the crack driving force (with respect to crack length) were, therefore, close to the levels required for unstable crack growth upon renucleation of crack growth in the layers adjacent to the 400-μm-thick vanadium layers.

Final failure of the vanadium layers in all the specimens that were examined occurred predominately by cleavage

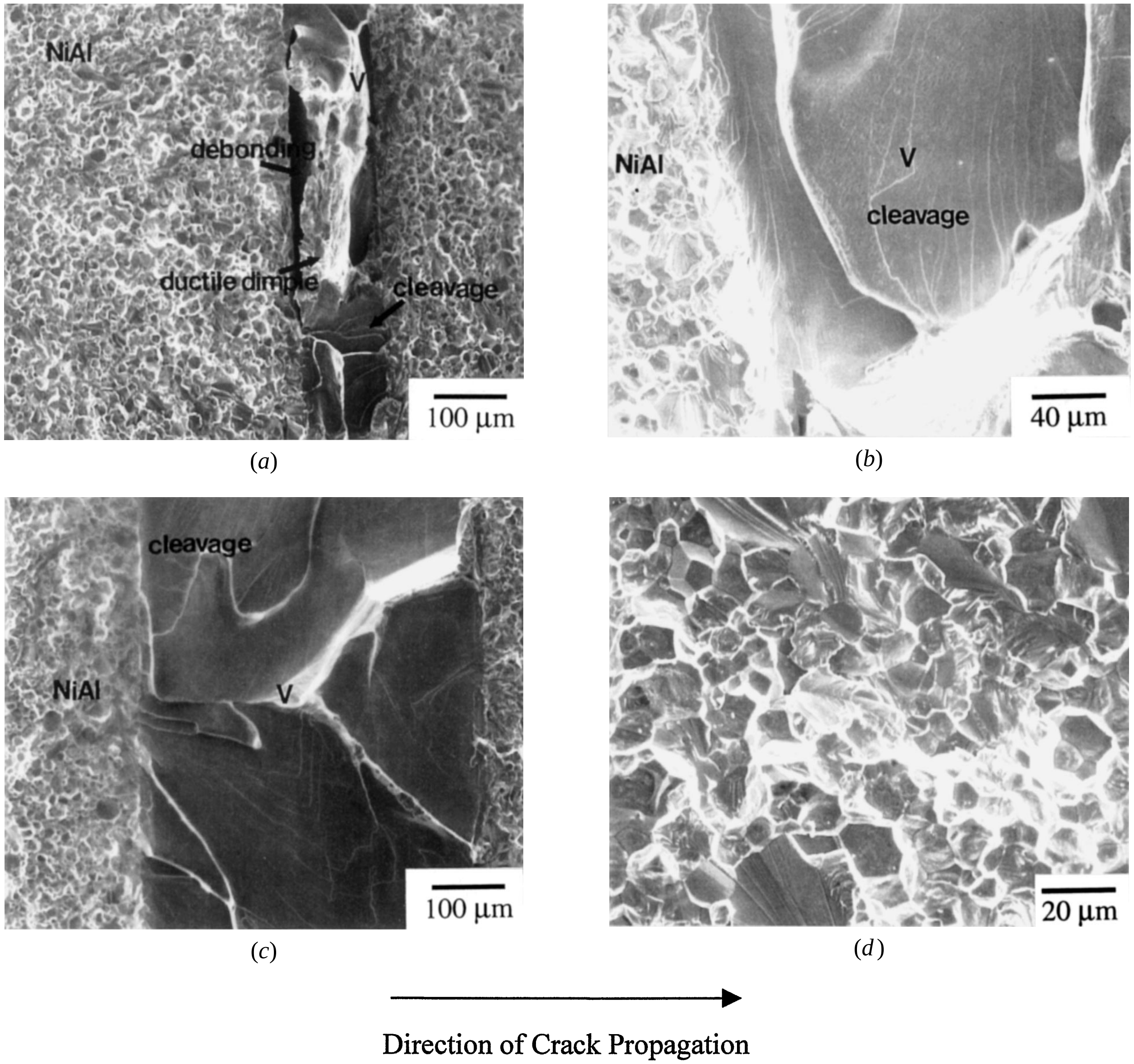

Fig. 9—Typical fracture modes in layered NiAl/V composite: (*a*) 100-μm-thick vanadium layer, (*b*) 200-μm-thick vanadium layer, (*c*) 400-μm-thick vanadium layer, and (*d*) NiAl matrix.

fracture, with some ductile dimpled fracture occurring in regions close to debonds (Figures 9(a) through (c)). It is postulated that the occurrence of cleavage in the middle of the vanadium layers was due to the relatively high levels of stress triaxiality, while the higher incidence of ductile dimpled fracture in the vicinity of the debonds was associated with the relaxation of constraint, *i.e.*, lower levels of stress triaxiality. In contrast, the NiAl matrix failed primarily by brittle intergranular fracture (Figure 9(d)).

The resistance curves obtained from experiments for NiAl composites reinforced with 100- and 200-μm-thick vanadium layers are shown in Figures 10(a) and (b), respectively. Each data point on the resistance curves corresponds to the position of a vanadium layer in front of the notch tip of the specimens. In both cases, the resistance curves increase significantly beyond the matrix toughness.

B. *NiAl/Nb-15Al-40Ti Composites*

The crack/microstructure interactions in the NiAl/Nb-15Al-40Ti microlaminates were somewhat complex, due to the polycrystalline nature of the Nb-15Al-40Ti layers. Unlike the V layers, the Nb-15Al-40Ti layers were prone to grain-boundary cracking during interactions with propagating cracks. This is shown clearly in Figures 11(a) and (b) for a specimen containing 100-μm-thick Nb-15Al-40Ti layers. The initial fatigue precrack appears to be on the left-hand side of the first layer (Figure 11(a)). However, it is possible that some segments of the crack have already intercepted the first Nb-15Al-40Ti layer across the thickness of the specimen. Consequently, the initiation toughness obtained after fatigue precracking is somewhat ill-defined, since it depends largely on the extent of the crack interactions

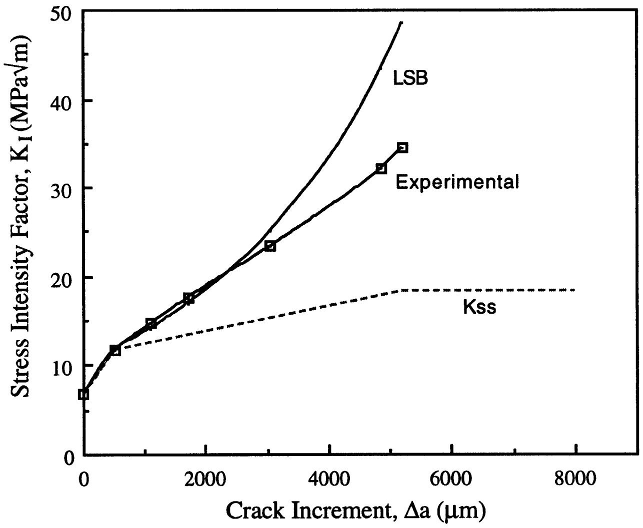

(*a*)

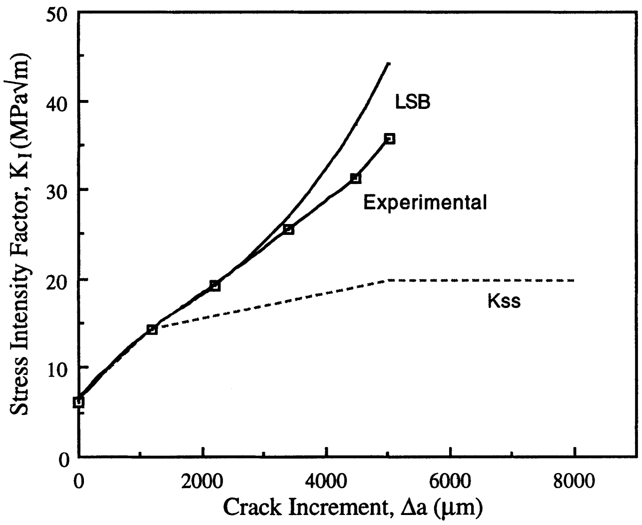

(*b*)

Fig. 10—Resistance curves obtained for NiAl/V composites from experiments and estimated from the LSB model: (*a*) 100-μm and (*b*) 200-μm vanadium laminates. K_{ss} is the steady-state toughness extracted from the weight function method.

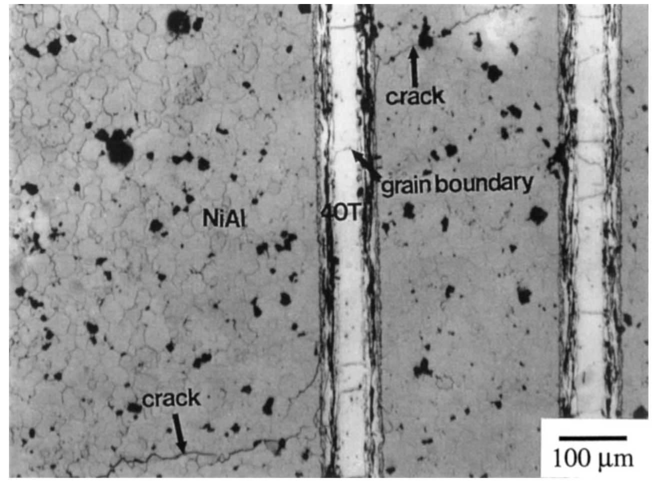

(*a*)

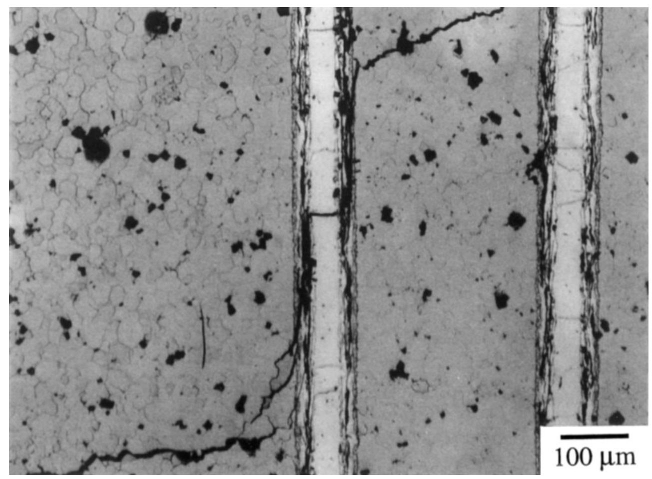

(*b*)

Direction of Crack Propagation

Fig. 11—Crack/microstructure interactions in NiAl composites reinforced with 100-μm-thick Nb-15Al-40Ti (40Ti) layer: (*a*) crack bridging and (*b*) bridging degradation by intergranular fracture across Nb-15Al-40Ti layers.

with the first ductile layer ahead of the initial crack tip. A renucleation toughness was, therefore, defined in an effort to identify a crack-initiation condition that was not subject to arbitrary differences in the initial crack/microstructure interactions. This was taken to correspond to the stress-intensity factor at which crack renucleation was observed ahead of the first ductile layer ahead of the initial crack tip.

Subsequent crack growth resulted in a bridged crack configuration (Figure 11(a)). However, unlike the bridging zones in the NiAl/V composites, the bridging zones in the NiAl/Nb-15Al-40Ti composites were degraded by intergranular cracking across the Nb-15Al-40Ti layers (Figure 11(b)). The overall bridging lengths in the NiAl/Nb-15Al-40Ti composite were, therefore, much less than those in the NiAl/V composites, in which the V layers remained intact prior to the onset of the catastrophic failure (Figure 12). Similar intergranular cracking phenomena in Nb-15Al-40Ti were observed in NiAl composites reinforced with 500- and 1000-μm-thick layers (Figure 13(b)). However, crack growth did not occur completely across the Nb-15Al-40Ti layers before the onset of catastrophic failure (Figure 13(b)). Crack bridging was also observed in the composites reinforced with 500-μm-thick Nb-15Al-40Ti layers (Figure 13(a)), but not in those with 1000-μm-thick Nb-15Al-40Ti layers. In the latter case, the crack renucleation from the first intercepting layer resulted in unstable crack growth and catastrophic failure. Prior to final fracture, there was considerable evidence of plastic stretching and slip bands in the Nb-15Al-40Ti layers (Figure 14). Furthermore, final fracture occurred by mixed-cleavage, ductile dimpled, and intergranular fracture in the Nb-15Al-40Ti layers (Figures 15(a) and (b)).

It is interesting to relate the aforementioned crack/microstructure interactions to the measured resistance curves presented in Figures 16(a) and (b). Only limited data are presented, due to the tendency of the specimens to undergo

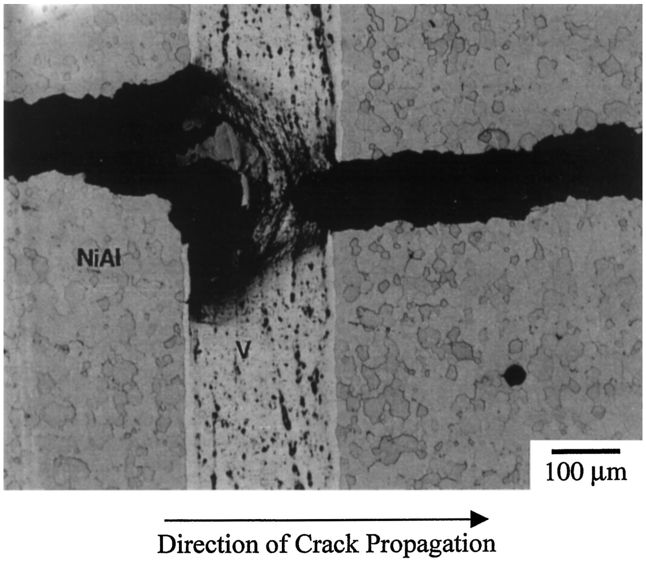

Fig. 12—The first vanadium layer intercepting propagating cracks prior to the catastrophic failure of NiAl composites reinforced with 200-μm-thick vanadium layers.

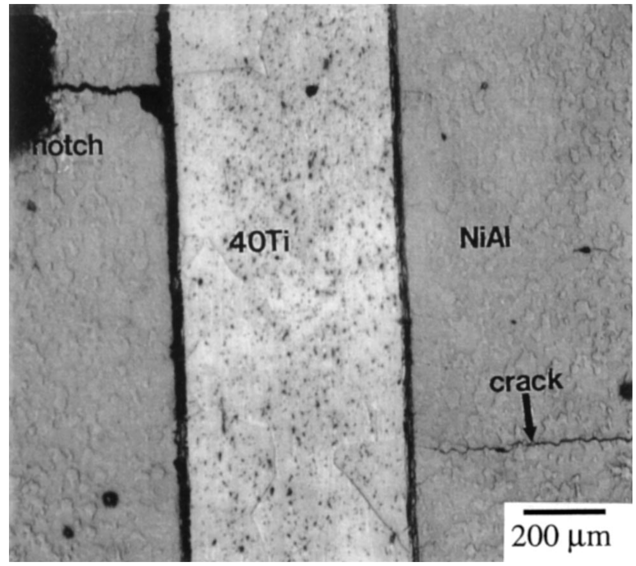

(*a*)

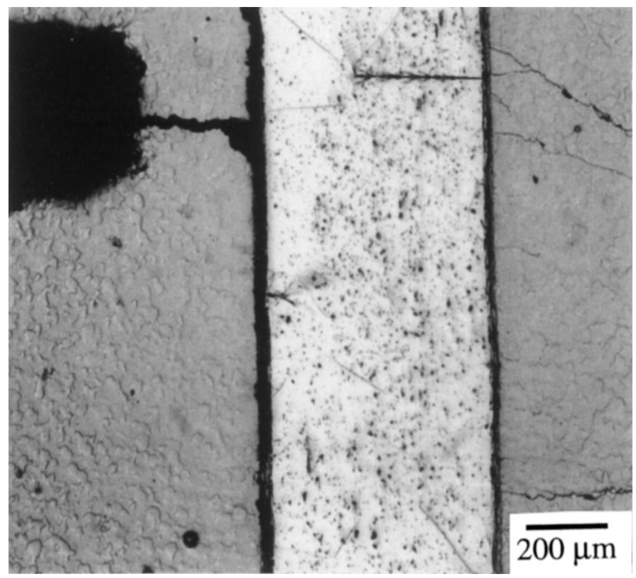

(*b*)

Direction of Crack Propagation

Fig. 13—Crack/microstructure interactions in NiAl composites reinforced with 500-μm-thick Nb-15Al-40Ti (40Ti) layer: (*a*) crack bridging and (*b*) intergranular fracture across Nb-15Al-40Ti layers.

unstable crack growth after a limited amount of crack extension. It is also important to note that each point on the resistance curves corresponds to the intersection of a propagating crack with an Nb-15Al-40Ti layer, or renucleation from the other side of the ductile layer. Furthermore, the Nb-15Al-40Ti layers are fractured (behind the crack tip) as the cracks propagate through subsequent NiAl layers. The measured resistance curves are, therefore, attributed largely to bridging by Nb-15Al-40Ti layers followed by intergranular fracture (behind the crack tip) with increasing bridge length. This is in contrast to the NiAl/V composites, in which the V layers remained intact prior to the onset of the catastrophic failure.

VI. DISCUSSION

A. *Modeling of LSB*

It is clear from the microscopic examination of the crack/layer interactions that crack tip shielding in NiAl/V and NiAl/Nb-15Al-40Ti composites occurred predominantly *via* crack bridging (Figures 7, 8, 11, and 13). It is, therefore, of interest to examine the shielding effects due to crack bridging. The LSB framework accounts for the weighted distribution of the bridging traction along a bridge zone (Eqs. [18] and [20]).

The remote stress-intensity factor required to cause crack growth under LSB conditions may, thus, be estimated from Eq. [17]. Note that K_i, the stress-intensity factor required for renucleation from the first layer that intercepts the propagating crack, is used instead of the matrix toughness, because bridging does not occur prior to matrix crack renucleation from the first layer that intercepts the crack. Furthermore, the variabilities in the measured values of K_i are generally significantly less than those in the initiation-toughness values associated with compression precracks, whose positions are less-well-defined across the specimen thickness, as shown in the case of NiAl/Nb-15Al-40Ti composites. This again indicates that K_i is a more appropriate term to use in Eq. [17]. The values of K_i obtained for the three layer thicknesses in each composite are summarized in Tables III and IV, respectively. These show that K_i increases with increasing layer thickness.

The prediction of K_{lsb} employs the traction function, which depends on the stress-stretch relationships determined from the experiments on the single-layer composite tensile tests. Here, $\sigma(x)$ is assumed to be a constant and can be equated to the yield stresses of the monolithic V and Nb-15Al-40Ti foils. The predicted LSB resistance curves are presented in Figures 10 and 16. Note that no LSB predictions were obtained for composites with 400-μm-thick vanadium layers and 1000-μm-thick Nb-15Al-40Ti layers, since bridging was

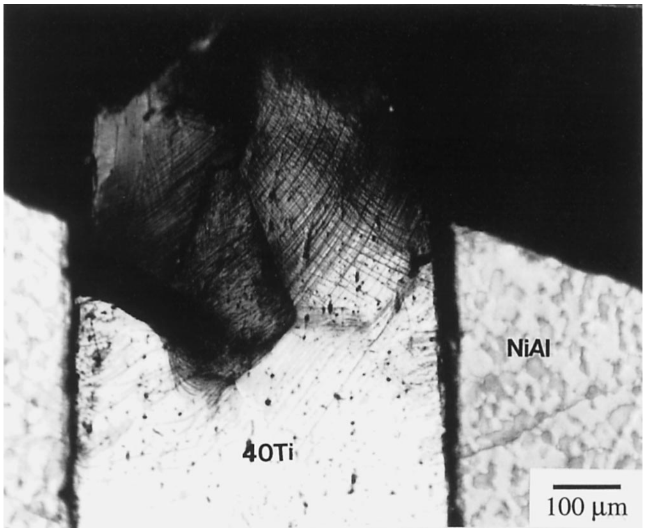

Fig. 14—Extensive plastic deformation observed in 500-μm-thick Nb-15Al-40Ti (40Ti) layers after the failure of NiAl/Nb-15Al-40Ti composites.

not observed in these specimens. As in prior studies on other intermetallic composite systems,[12–14,33] the LSB predictions are comparable to the measured resistance curves, except at high Δa levels, where the levels of constrained yielding of the vanadium layers may be very different. Improved weighting functions may also be needed to account for the distribution of layer tractions at high levels of Δa. In any case, similar LSB results have been reported in previous studies on other ductile phase–toughened intermetallic matrices such as $MoSi_2$/Nb,[33] Nb_3Al/Nb,[12,13,14] and TiAl/TiNb.[18]

Since neither the measured resistance curves nor the LSB resistance curves exhibit steady-state toughness values, an attempt has been made to obtain the specimen-independent steady-state toughness (K_{ss}) from Eqs. [15] through [17]. This was achieved by assuming a specimen width that is significantly greater than the length of the bridge zone, *i.e.*, simulating small-scale bridging conditions artificially. This approach, which was first applied by Bloyer *et al.*[13,14] to Nb_3Al/Nb layered composites, estimates the small-scale steady-state toughness by simulating the effects of larger specimen widths in Eqs. [15] through [17]. The estimates of K rapidly converge to an asymptotic solution as the specimen width is increased artificially toward infinity. This has the advantage of providing intrinsic toughness values that are essentially independent of specimen geometry differences. The calculated steady-state toughness values for NiAl/V and NiAl/Nb-15Al-40Ti composites are listed in Tables III and IV, respectively. Note that the values of K_{ss} increase with increasing layer thickness (Tables III and IV).

It is interesting to compare the previously predicted steady-state toughness to theoretical estimates of ΔK_b from Eqs. [13] and [14]. The results are shown in Tables III and IV. The material parameters that were used in the modeling are summarized in Table II. The analysis assumes that the ductilities of the ductile layers are somewhat degraded due to interdiffusion phenomena and constrained yielding. In any case, the predicted steady-state toughness levels from Eqs. [13] and [14] are generally comparable to those extrapolated from the weight-function method (Eqs. [15] through [17]). The modeling framework presented in Eqs. [13] and

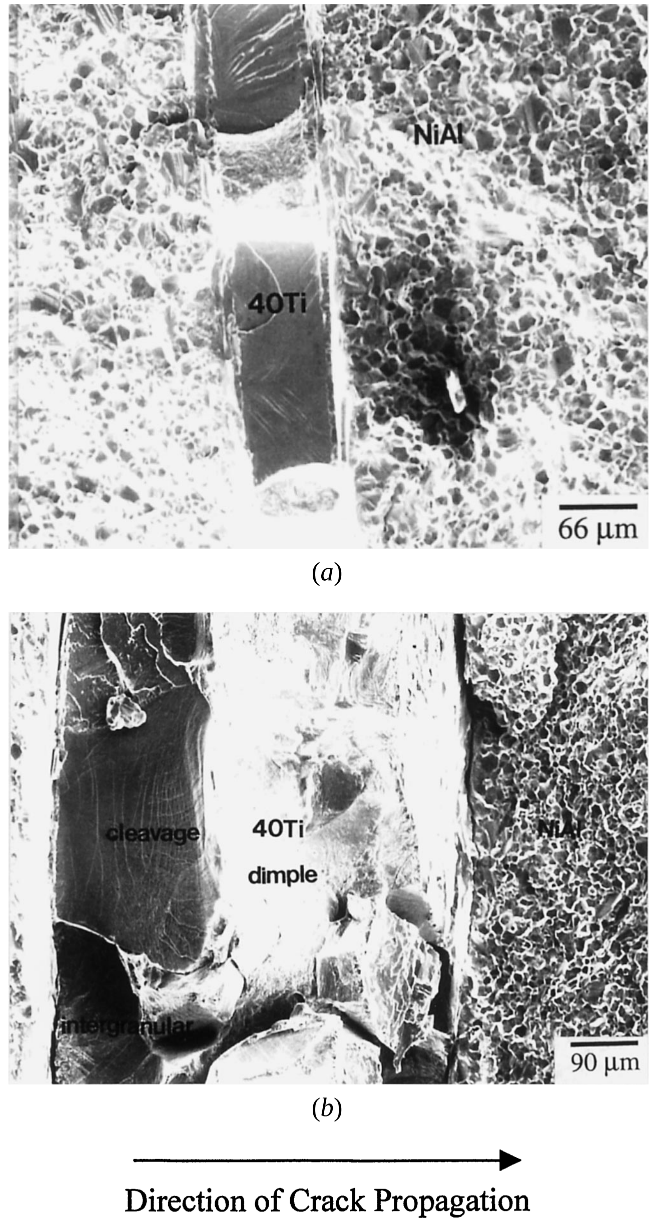

Fig. 15—Typical fracture modes in layered NiAl/Nb-15Al-40Ti (40Ti) composite: (*a*) 100-μm-thick Nb-15Al-40Ti layer and (*b*) 500-μm-thick Nb-15Al-40Ti layer.

[14], therefore, appears to provide reasonably accurate estimates of the fracture toughness of the model microlaminates that were examined in this study.

The previous modeling framework has general implications for the design of damage-tolerant multilaminates. First, it may be used to obtain specimen-independent measures of the intrinsic fracture toughness corresponding to a particular composite geometry. This greatly simplifies the analyses of fracture-critical events. It also facilitates the selection of ductile-layer compositions and geometries that are most likely to give rise to improved intrinsic toughness. Furthermore, in cases where geometry-dependent fracture-mechanics analyses are needed, the simple linear superposition framework discussed in Section II can be used to estimate the resistance-curve behavior of "designer" composites prior to specimen fabrication. This could significantly reduce the

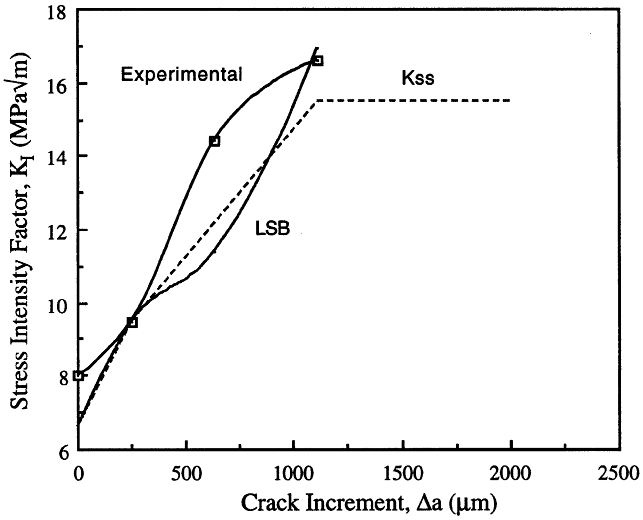

(*a*)

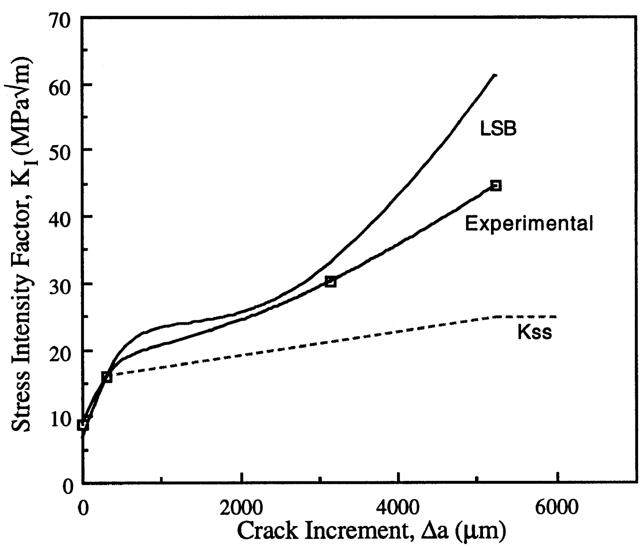

(*b*)

Fig. 16—Resistance curves obtained for NiAl/Nb-15Al-40Ti composites from experiments and estimated from the LSB model: (*a*) 100-μm and (*b*) 500-μm Nb-15Al-40Ti laminates. K_{ss} is the steady-state toughness extracted from the weight function method.

Table III. Comparison of Initiation Toughness and Steady-State Toughness for NiAl/V Laminate

V Layer Thickness	Initiation Toughness K_i (MPa$\sqrt{m}$)	Steady-State Toughness K_{ss} (MPa$\sqrt{m}$): Predicted by Weight Function Method	Steady-State Toughness K_{ss} (MPa$\sqrt{m}$): Predicted by Eqs. [13] and [14]
100 μm	11.8	18.4	17.4
200 μm	14.4	19.8	23.6
400 μm	20.9	—	—

number of iterations that are needed for the design of composite geometries with optimal resistance to the growth of cracks. Finally, since the previous analyses do not involve iterative schemes that may not converge, the toughening predictions only require limited computational effort for the design of damage-tolerant microlaminates.

Table IV. Comparison of Initiation Toughness and Steady-State Toughness for NiAl/Nb-15Al-40Ti Laminate

Nb-15Al-40Ti Layer Thickness	Initiation Toughness K_i (MPa$\sqrt{m}$)	Steady-State Toughness K_{ss} (MPa$\sqrt{m}$): Predicted by Weight Function Method	Steady-State Toughness K_{ss} (MPa$\sqrt{m}$): Predicted by Eqs. [13] and [14]
100 μm	9.5	15.4	14.7
500 μm	16.1	24.6	30.0
1000 μm	22.3	—	—

B. *Comparison to Other Layered Systems*

The current results are consistent with the results of Bloyer *et al.*,[13] who also showed that the intrinsic steady-state toughness values increase with increasing layer thickness in ductile layer–toughened brittle matrix composites. The aforementioned trends, therefore, appear to apply generally to brittle matrix composites (microlaminates) reinforced with ductile layers. However, they may not apply to nanolaminates, in which toughening may be controlled by dislocation/boundary interactions and pileups at interfaces.[34,35,36] Such nanoscale composites may offer some opportunities for toughening by layer refinement. However, the limited amount of experimental data published for such systems[37,38] suggest that the fracture-toughness levels in nanolaminates are limited to levels between ~1 and 5 MPa$\sqrt{m}$. Microlaminate architectures, therefore, appear to offer greater opportunities for the design of tougher composites than nanolamiantes, at least within the near term. This is particularly encouraging, since the microlaminates are relatively easy to fabricate compared to nanolaminates. The larger dimensions in microlaminates can also be readily controlled by varying the foil dimensions or the amount of powder that is used in the lay-up of the composites.

C. *Implications for Damage-Tolerant Design*

The two model systems examined in the current article consistently show that significant resistance-curve behavior can be engineered in brittle NiAl composites reinforced with ductile layers with thicknesses ranging from 100 to 1000 μm. Similar improvements in microlaminate fracture toughness have also been reported by Kajuch *et al.*[20] for niobium silicide composites reinforced with ductile Nb layers. Ye *et al.*[33] and Shaw and Abbaschian[21] have also demonstrated that $MoSi_2$/Nb microlaminates exhibit large improvements in fracture toughness/resistance-curve behavior which are comparable to those observed in this study on NiAl microlaminates.

However, none of the previous systems are suitable for applications as structural materials in high-temperature systems. This is due largely to the fact that their "true" initiation-toughness (from the precracks) levels are still close to those of the brittle matrix materials. Subsequent resistance-curve behavior is also associated largely with intermittent crack/layer interactions, in which relatively fast crack growth rates

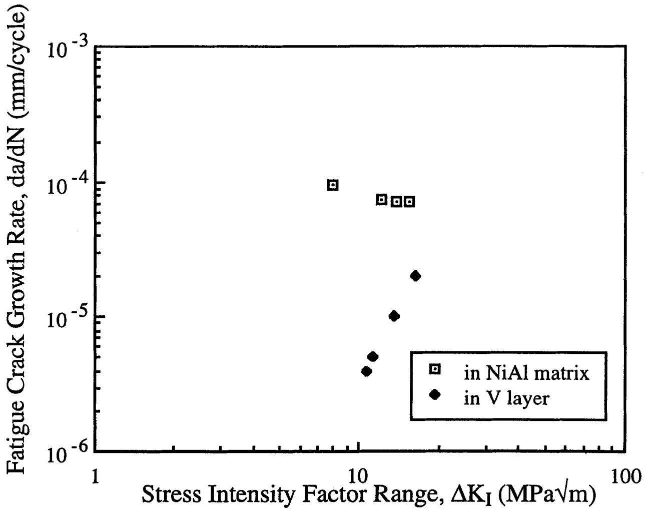

Fig. 17—Fatigue crack growth rate data for NiAl composites reinforced with 200-μm-thick vanadium layers.

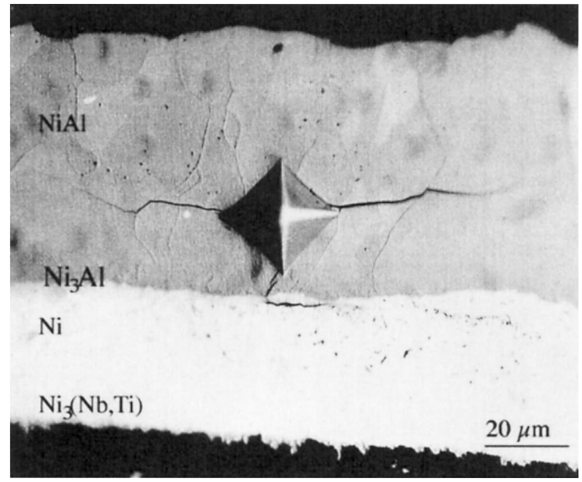

Fig. 19—Indentation crack growth resistance by ductile nickel layer of a multilayered $NiAl/Ni_3Al/Ni/Ni_3(Nb,Ti)$ coating on Nb-15Al-40Ti alloy substrate.[40]

occur between the individual ductile layers.[4,14] This is especially true under cyclic loading, where the crack growth rates are particularly fast compared to those in ductile layers.[4,14] One example of the relatively fast growth rates in the brittle NiAl layers is shown in Figure 17, in which fatigue crack growth-rate data obtained for NiAl/V microlaminates are compared. Note that the fatigue crack growth rates are relatively slow in the ductile vanadium layers, where fatigue crack growth occurs by classical crack-tip blunting mechanisms[39] that give rise to striation formation (Figure 18(a)). In contrast, fast fatigue crack growth rates occur in the NiAl layers, where crack growth occurs predominantly by intergranular fracture, as shown in Figure 18(b).

The very fast crack growth rates in the brittle matrix materials, therefore, result in average fatigue crack growth rates in the composites/microlaminates which are too fast for damage-tolerant structural applications in high-temperature systems such as aeroengines and land-based engines. However, it is possible that the layered composite architectures (microlaminates) may be used in the design of damage-tolerant coatings that undergo progressive, but controlled, degradation, due to combinations of cracking and oxidation phenomena (Figure 19).[40] Further work is needed to explore the possible design of novel multilayered coatings within this framework.

VII. CONCLUSIONS

The fracture toughness/resistance-curve behavior of two model microlaminate (NiAl/V and NiAl/Nb-15Al-40Ti) systems has been investigated in this study. The salient conclusions arising from the study are summarized as follows.

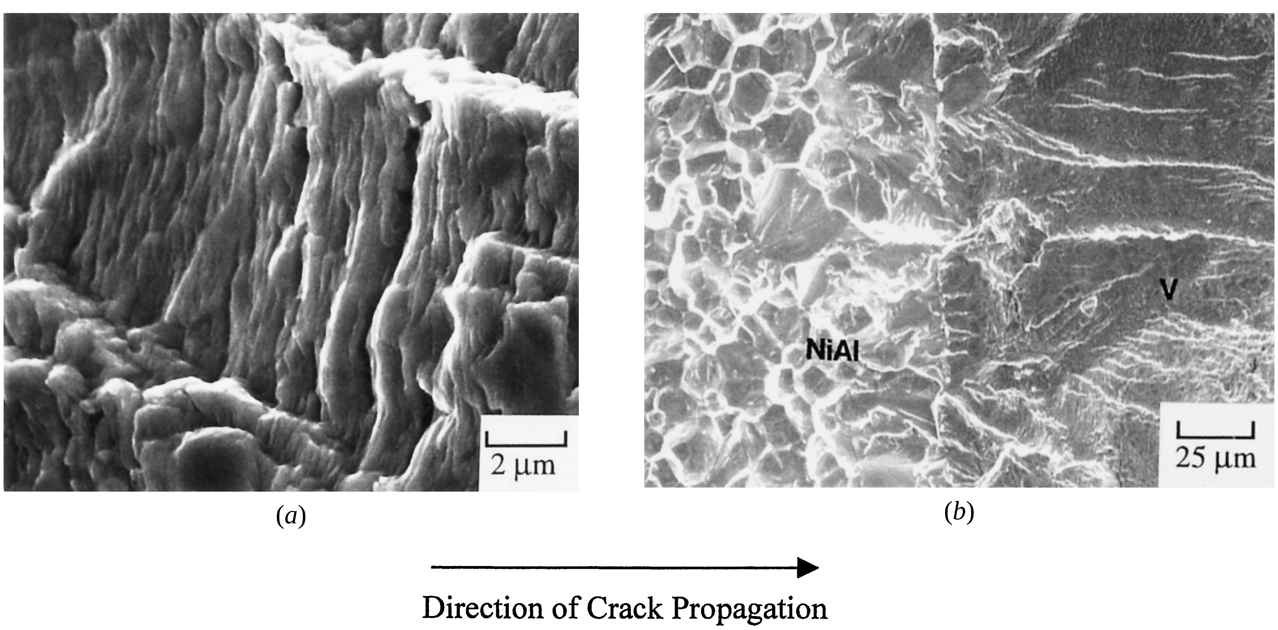

Fig. 18—Typical fracture modes in NiAl composites reinforced with 200-μm-thick vanadium layers under cyclic loading: (a) fatigue striations in vanadium layer and (b) intergranular fracture in NiAl matrix.

1. The specimen-independent intrinsic steady-state fracture toughness of ductile-reinforced microlaminates increases with the increasing thickness of the ductile layers. The improved intrinsic toughness values and the observed resistance-curve behavior are attributed largely to the shielding effects of crack bridging by the ductile layers. Estimates of the resistance curves obtained from layer bridging models are also in general agreement with the measured resistance curves.

2. The crack/layer interactions in the NiAl/V composites are similar for the three vanadium layer thicknesses (100, 200, and 400 μm) examined in this study. The resistance-curve behavior in these systems is associated with the following sequence of events: crack retardation by the ductile vanadium layers; slip-band nucleation ahead of the crack tip in the vanadium layers; renucleation of crack growth in adjacent NiAl layers; and crack bridging by the uncracked vanadium layers behind the crack tip. This sequence is repeated until unstable crack growth occurs during crack renucleation in the adjacent NiAl layers. The increase in the stress-intensity factor required for renucleation also increases with an increasing ductile vanadium layer thickness. However, renucleation is most likely to be followed by unstable crack growth/catastrophic failure in the case of the composite reinforced with the thicker layers.

3. Similar phenomena are observed in the NiAl/Nb-15Al-40Ti composites. However, the crack/layer interactions in these systems are more complex, due to the relative weakness of the grain boundaries in the Nb-15Al-40Ti layers and the interfacial reaction that occurs between the NiAl and Nb-15Al-40Ti layers. The former gives rise to intergranular crack growth across the Nb-15Al-40Ti layers, while the latter gives rise to limited debonding. The intergranular crack growth across the Nb-15Al-40Ti layers also tends to decrease the sizes of the bridging zones, since they lead to premature failure of the Nb-15Al-40Ti layers. Nevertheless, the NiAl/Nb-15Al-40Ti composites exhibit significant resistance-curve behavior. The measured resistance curves are also predicted by fracture-mechanics models, in which the actual bridging and crack/layer dimensions are used.

4. In spite of the observed and predicted resistance curve behavior, the model microlaminate systems investigated in this study are not recommended for future consideration for possible structural applications in high-temperature systems. This is due largely to the relatively low "initiation" toughness levels and the fast crack growth rates in the brittle NiAl layers. The average crack growth rates in the composites/microlaminates are considered to be too fast for potential structural applications. However, it is possible that the layered composite configurations may be useful in high-temperature coatings, especially in systems where the model ductile layers are replaced by oxidation-resistant alloys such as nickel-based superalloys. Further work is clearly needed to explore such possibilities.

ACKNOWLEDGMENTS

The research on NiAl/V composites was supported by the Division of Mechanics and Materials, National Science Foundation, with Dr. Dan Davis as program monitor. The research on NiAl/Nb-15Al-40Ti composites was supported by the Office of Naval Research, with Dr. George Yoder as program monitor. The authors are grateful to Drs. Davis and Yoder for their encouragement and support. Appreciation is also extended to Professors Peter Anderson, Anthony Evans, John Hutchinson, Zhigang Suo, Rob Ritchie, Frank Zok, and Bob Odette, and Drs. Ming He and Dan Bloyer for useful technical discussions. The authors are also grateful to Mrs. Betty Adam and Dr. Seyed Allameh for assistance with final preparation of the article.

REFERENCES

1. V.D. Kristic, P.S. Nicholson, and R.G. Hoagland: *J. Am. Ceram. Soc.*, 1981, vol. 64, pp. 499-504.
2. V.D. Kristic: *Phil. Mag.*, 1983, vol. 48, pp. 695-708.
3. W.O. Soboyejo, K.T. Venkateswara Rao, S.M.L. Sastry, and R.O. Ritchie: *Metall. Trans. A*, 1993, vol. 24A, pp. 585-99.
4. W.O. Soboyejo, F. Ye, L.-C. Chen, N. Bahtish, D.S. Schwartz, and R.J. Lederich: *Acta Mater.*, 1996, vol. 44, pp. 2027-41.
5. P. Ramasundaram, R. Bowman, and W.O. Soboyejo: *Mater. Sci. Eng. A*, 1998, vol. A248, pp. 132-46.
6. P.A. Mataga: *Acta Metall.*, 1989, vol. 37, pp. 3349-59.
7. M.F. Ashby, F.J. Blunt, and M. Bannister: *Acta Metall.*, 1989, vol. 37, pp. 1847-57.
8. H.C. Cao, B.J. Dalgleish, H.E. Deve, C. Elliott, A.G. Evans, R. Mehrabian, and G. R. Odette: *Acta Metall.*, 1989, vol. 37, pp. 2969-77.
9. H.E. Deve and M.J. Maloney: *Acta Metall. Mater.*, 1991, vol. 39, pp. 2275-84.
10. M. Bannister, H. Shercliff, G. Bao, F. Zok, and M.F. Ashby: *Acta Metall. Mater.*, 1992, vol. 40, pp. 1531-37.
11. F.E. Heredia, M.Y. He, G.E. Lucas, A.G. Evans, H.E. Deve, and D. Konitzer: *Acta Metall. Mater.*, 1993, vol. 41, pp. 505-11.
12. D.R. Bloyer, K.T. Venkateswara Rao, and R.O. Ritchie: *Mater. Sci. Eng. A*, 1996, vol. A216, pp. 80-90.
13. D.R. Bloyer, K.T. Venkateswara Rao, and R.O. Ritchie: *Metall. Mater. Trans. A*, 1998, vol. 29A, pp. 2483-96.
14. D.R. Bloyer, K.T. Venkateswara Rao, and R.O. Ritchie: *Metall. Mater. Trans. A*, 1999, vol. 30A, pp. 633-42.
15. M.Y. He, F.E. Heredia, D.J. Wissuchek, M.C. Shaw, and A.G. Evans: *Acta Metall. Mater.*, 1993, vol. 41, pp. 1223-28.
16. X.F. Chen, D.R. Johnson, R.D. Noebe, and B.F. Oliver: *J. Mater. Res.*, 1995, vol. 10, pp. 1159-70.
17. S.M. Joslin, X.F. Chen, B.F. Oliver, and R.D. Noebe: *Mater. Sci. Eng. A*, 1995, vol. A196, pp. 9-18.
18. G.R. Odette, B.L. Chao, J.W. Sheckherd, and G.E. Lucas: *Acta Metall. Mater.*, 1992, vol. 40, pp. 2381-89.
19. P.R. Subramanian, M.G. Mendiratta, and D.B. Miracle: *Metall. Mater. Trans. A*, 1994, vol. 25A, pp. 2769-81.
20. J. Kajuch, J. Short, and J.J. Lewandowski: *Acta Metall. Mater.*, 1995, vol. 43, pp. 1955-67.
21. L. Shaw and R. Abbaschian: *Acta Metall. Mater.*, 1994, vol. 42, pp. 213-23.
22. M. Li, R. Wang, N. Katsube, and W.O. Soboyejo: *Scripta Mater.*, 1999, vol. 40, pp. 397-402.
23. F. Ye, C. Mercer, and W.O. Soboyejo: *Metall. Mater. Trans. A*, 1998, vol. 29A, pp. 2361-74.
24. W.O. Soboyejo, J. DiPasquale, F. Ye, C. Mercer, T.S. Srivatsan, and D.G. Konitzer: *Metall. Mater. Trans. A*, 1999, vol. 30A, pp. 1025-37.
25. B. Budiansky, J.C. Amazigo, and A.G. Evans: *J. Mech. Phys. Solids*, 1988, vol. 36, pp. 167-87.
26. L.R.F. Rose: *J. Mech. Phys. Solids*, 1987, vol. 35, pp. 383-405.
27. K.L. Johnson: *Contact Mechanics*, Cambridge University Press, Cambridge, United Kingdom 1985.
28. H. Tada, P.C. Paris, and G.R. Irwin: *The Stress Analysis of Cracks Handbook*, Del Research, St. Louis, MO, 1985.
29. F. Zok and C.L. Hom: *Acta Metall. Mater.*, 1990, vol. 38, pp. 1895-1904.
30. B.N. Cox and C.S. Lo: *Acta Metall. Mater.*, 1992, vol. 40, pp. 69-80.
31. B.N. Cox and L.R.F. Rose: *Mech. Mater.*, 1996, vol. 22, pp. 249-63.
32. T. Fett and D. Munz: *Stress Intensity Factors and Weight Functions for One-Dimensional Cracks*, Institut fur Materialforschung, Kernforschungszentrum, Karlsryhe, Germany, 1994.
33. F. Ye, M. Li, and W.O. Soboyejo: *J. Am. Ceram. Soc.*, 1999, vol. 82, pp. 2460-64.
34. S. Muju, P.M. Anderson, and D.A. Mendelsohn: *Acta Mater.*, 1998, vol. 46, pp. 5385-97.
35. D.L. Davidson: Southwest Research Institute, San Antonio, TX,

unpublished research, 1998.
36. D. Van Heerden, A.J. Gavens, T. Foecke, and T.P. Weihs: *Mater. Sci. Eng. A*, 1999, vol. A261, pp. 212-16.
37. H.C. Cao, J.P. Lofvander, A.G. Evans, R.G. Rowe, and D.W. Skelly: *Mater. Sci. Eng. A*, 1994, vol. A185, pp. 87-95.
38. J. Heathcote, G.R. Odette, and G.E. Lucas: *Acta Mater.*, 1996, vol. 44, pp. 4289-99.
39. C. Laird and G.C. Smith: *Phil. Mag.*, 1962, vol. 8, pp. 847-57.
40. Y. Li, W.O. Soboyejo, and R.A. Rapp: *Metall. Mater. Trans. B*, 1999, vol. 30B, pp. 495-504.